energies

MDPI

Article

Effect on Torque and Thrust of the Pointed Tip Shape of a Wind Turbine Blade

Kyoungsoo Lee [1], Shrabanti Roy [2], Ziaul Huque [2,*], Raghava Kommalapati [3] and SangEul Han [4]

[1] Center for Energy and Environmental Sustainability, Incohen Co., Seoul 05510, Korea; lks1838@naver.com
[2] Center for Energy and Environmental Sustainability (CEES), Department of Mechanical Engineering, Prairie View A&M University (PVAMU), Prairie View, TX 77446, USA; shroy@pvamu.edu
[3] Center for Energy and Environmental Sustainability, Department of Civil & Environmental Engineering, Prairie View A&M University (PVAMU), Prairie View, TX 77446, USA; rrkommalapati@pvamu.edu
[4] School of Architecture, Department of Architectural Engineering, Inha University, Inchoen 402-751, Korea; hsang@inha.ac.kr
* Correspondence: zihuque@pvamu.edu; Tel.: +1-936-261-9957

Academic Editor: Frede Blaabjerg
Received: 11 November 2016; Accepted: 2 January 2017; Published: 11 January 2017

Abstract: This paper presents the effect of the tip shape of a wind turbine blade on aerodynamic forces, including the effects of separation, transition and stall. A National Renewable Energy Laboratory (NREL) Phase-VI wind turbine blade was used, in which the shape of the tip was modified to a pointed tip. Computational fluid dynamics (CFD) simulations were employed for the analysis and the results were compared with the original NREL blade CFD and experimental data using ANSYS CFX (Ansys Inc., Delaware, PA, USA). To predict the separation and separation-induced transition on both near wall and far away, the shear-stress-transport (SST) Gamma-Theta turbulent model was used. The stall onset of a 20° angle of attack and its effects were also analyzed and presented. The value of torque with the pointed tip blade was found to be 3%–8% higher than the original NREL blade showing the benefit of the pointed tip. Normal force coefficient is lower at the tip for the pointed tip blade, which results in lower deformation of the blade. It was found that the pointed-tip blade is more efficient in terms of generating torque than the original NREL Phase-VI blade in the dynamic stall region of 10–15 m/s wind speeds.

Keywords: wind energy; wind turbine blade; pointed tip blade; National Renewable Energy Laboratory (NREL) Phase VI; shear-stress-transport (SST) Gamma-Theta turbulent model; separation and transition

1. Introduction

Wind turbines are gaining popularity because they represent an eco-friendly source of power. Considerable amounts of research on increasing their power-generation capacity is currently being carried out. Wind can be considered as a form of solar energy because it is caused by the uneven heating of the atmosphere by the Sun, irregularities of the Earth's surface and the rotation of the Earth. A wind turbine is the device which is used to extract energy from the wind. The design of wind turbine blades and their power-generation efficiency is currently a major research area.

Accurate aerodynamic-force evaluation is important for three-dimensional (3D) wind-turbine blade design. The performance of a 3D blade depends greatly on its aerodynamic-force characteristics. To evaluate these characteristics, wind-tunnel tests were conducted at the NASA Research Center for a two-dimensional (2D) airfoil [1,2] and a 3D wind-turbine blade [3,4].

The National Renewable Energy Laboratory (NREL) conducted 2D wind-tunnel tests to elucidate the sectional aerodynamic forces. A S809 airfoil was used for these tests [3,4]. Wind-turbine design codes are based on aerodynamic forces derived from 2D wind-tunnel airfoil test results. Practical

wind-turbine blades undergo many complex aerodynamic phenomena that are difficult to replicate in the 2D wind tunnel tests.

In field tests, wind turbines exhibit severe unsteady 3D transient effects, which 2D analysis fails to predict. Thus, to induce an accurate 3D effect on a turbine blade, it was necessary to build a full-scale 3D wind-turbine blade. After doing considerable research work, the Phase-VI wind-turbine blade made by NREL was selected for the 3D wind-tunnel tests in the NASA Ames Research Center.

These tests captured 3D aerodynamic effects which are relevant to practical field cases. As a result many researchers have used these 3D Phase VI wind-turbine blade data to verify their findings. The 3D wind-tunnel tests were able to measure and identify most of the aerodynamic effects- including stall, turbulence, and separation—at high wind speeds.

Although the 3D wind-tunnel tests can describe most of the aerodynamic effects on a wind-turbine blade, it is not possible to use a wind tunnel to optimize every wind-turbine blade performance. Owing to this limitation, the blade-element momentum (BEM) theory was formulated, which employs 2D wind-tunnel test data to calculate 3D aerodynamic effects to design and optimize wind-turbine blades [5–7]. Although BEM can calculate 3D wind-turbine blade results, it cannot perfectly predict aerodynamic effects such as stall and separation, because it employs 2D data.

Even though BEM was the first and is a reliable process, due to its limitations in capturing 3D effects, recently newly generated numerical methods like the vortex lattice method (VLM) [8] and computational fluid dynamics (CFD) [9–18] are becoming popular for the calculation of aerodynamic forces. The vortex-lattice method is divided into prescribed-wake methods and free-wake methods for its calculation. However viscous effects and turbulence effects are neglected in these methods [10] which are important features in practical wind turbine blade calculation. To address all the challenges of practical conditions of a turbine blade, wind energy community currently started to use CFD. The earliest use of CFD was in predicting 2D flows around a span wise section of a wind turbine blade. However, with the availability of increased computing power, it has been used on all scales: from the airfoil boundary layer to the atmospheric boundary layer. The majority of models are based on the incompressible Reynolds-Averaged Navier-Stokes (RANS) model.

CFD code has been used to model several equations that predict the effects of boundary conditions under turbulence and their effect on the wall function and integrated boundary function. Several model equations have yielded proper predictions for both near-wall and larger-scale boundary-effect cases. A correlation based model, SST Gamma-Theta, has been introduced in this work which can predict near wall and larger scale boundary effects and can accurately measure the viscous sublayer boundary flow and transitional flow [19,20]. This model is employed in this work owing to its more precise prediction of stall, separation, and transition effects near the boundary [21,22].

The blade shape is a very important criterion in wind-turbine blade design. Power generation is found to be highly sensitive to even a minor change in the shape of the blade, especially in the region near the blade's tip. The region near the tip greatly influences the aerodynamic force along the span and hence the power. The design of a blade, as in most engineering solutions, is a complex compromise. The shape of the tip of a wind turbine blade is currently getting priority in blade design research. Although research has been performed on the effects of the pointed-tip blade shape, the detailed flow characteristics (separation or transition) and aerodynamic-force characteristics of the pointed-tip blade have not yet been demonstrated successfully [15–18].

Thus, in the present work, a pointed-tip blade was employed to evaluate the aerodynamic forces and their effects on stall and flow separation using CFD. The SST Gamma-Theta turbulent-transition model was used to simulate the airflow around a 3D NREL Phase-VI wind-turbine blade. To investigate the characteristics and advantages of the pointed tip, the blade geometry of the tip section of NREL Phase-VI blade was changed from the original shape by decreasing the chord length. The design was implemented using an ANSYS 3D geometry modeler. A large number of meshes were generated because a high-quality mesh allows better prediction. The Y+ value was less than one for accurately obtaining the effects of the separation and transition in the near wall of the blade in low-Reynold

number flow [18]. The ANSYS CFX software was used for the simulation. The sectional and overall changes in aerodynamic forces were examined under several wind speed conditions. The results were compared with the CFD and experimental results of the original NREL blade to show the advantages of pointed tip blade.

2. Blade Geometry and Methodology

The NREL Phase-VI wind turbine was developed at the NASA Ames Research Center. It was made with realistic rotating blade geometry under closely matched conditions of dynamic similarity and in the presence of strictly controlled inflow conditions. This airfoil was optimized to improve wind energy power production and is less sensitive to leading edge roughness [4]. The blade design was optimized on annual energy capture subject to the design constraints imposed for the instrumentation [22]. This NASA Ames facility was designed to provide accurate and reliable experimental measurements with a high spatial and temporal resolution. The tower height and blade diameter of NREL UAE Phase-VI wind turbine was 12.5 and 10.6 m, respectively, as shown in Figure 1.

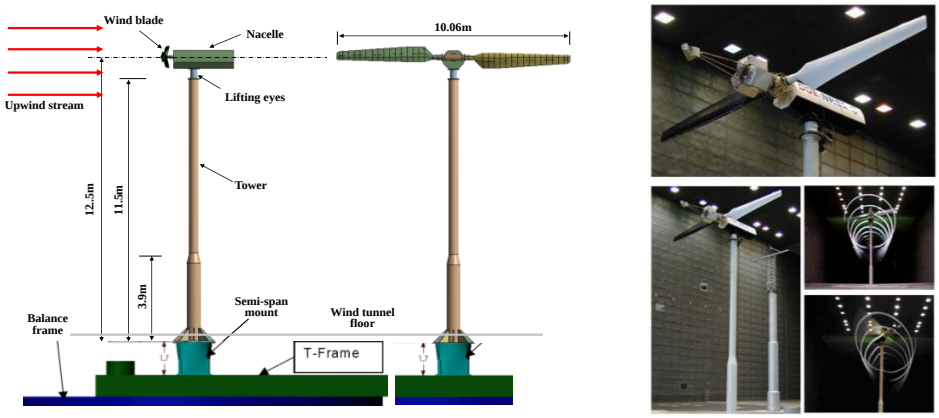

Figure 1. Full scale National Renewable Energy Laboratory (NREL) Phase VI wind turbine blade and its dimensions [3,4].

The NREL Phase-VI blade is made of S809 which is a 21% thick laminar-flow airfoil [2]. The blade was divided into five sections along the span-wise direction. Several pressure taps were used on each section for testing purpose as shown in Figure 2a,b.

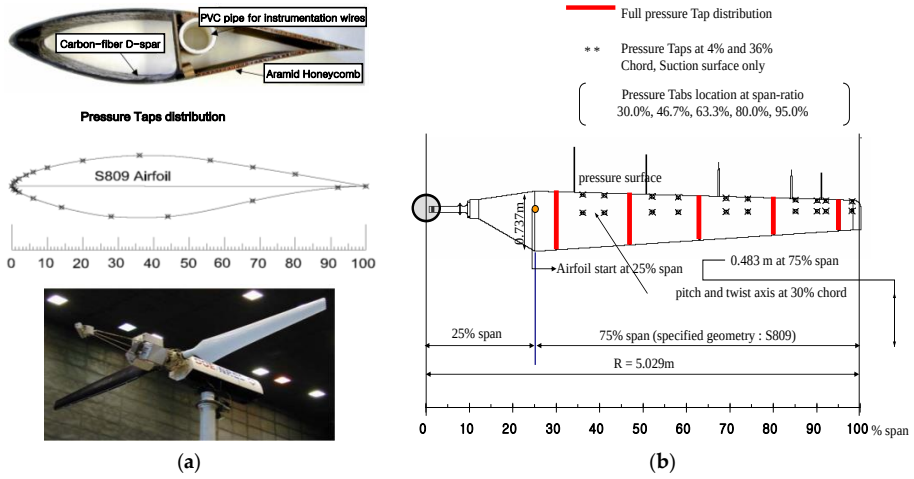

Figure 2. Sectional and span-wise pressure tap locations on NREL Phase VI Blade [3,4]. (**a**) Sectional pressure taps distribution; and (**b**) span wise pressure tap distribution.

The design process used extensive trade-off studies that considered nonlinear taper and twist, and additional airfoils. Based on that study, a linear taper and a nonlinear twist distribution is used for S809 airfoil from root to tip. In the current study the same twist distribution was kept for the entire blade. In case of taper, the only change was in the last 10% of the span where the shape of the tip changed to a pointed tip shape as shown in Figure 3a,b [4]. The blade chord was tapered from 0.737 m at 0.25 R (where R is the span of the blade) to 0.356 m at the tip. The twist decreased from 20.0° at 0.25 R to −2.0° at the tip. The blade was pitched about an axis located at 30% of the chord length along the leading edge and centered between the blade's upper and lower surfaces at that chord location as shown in Figure 3c.

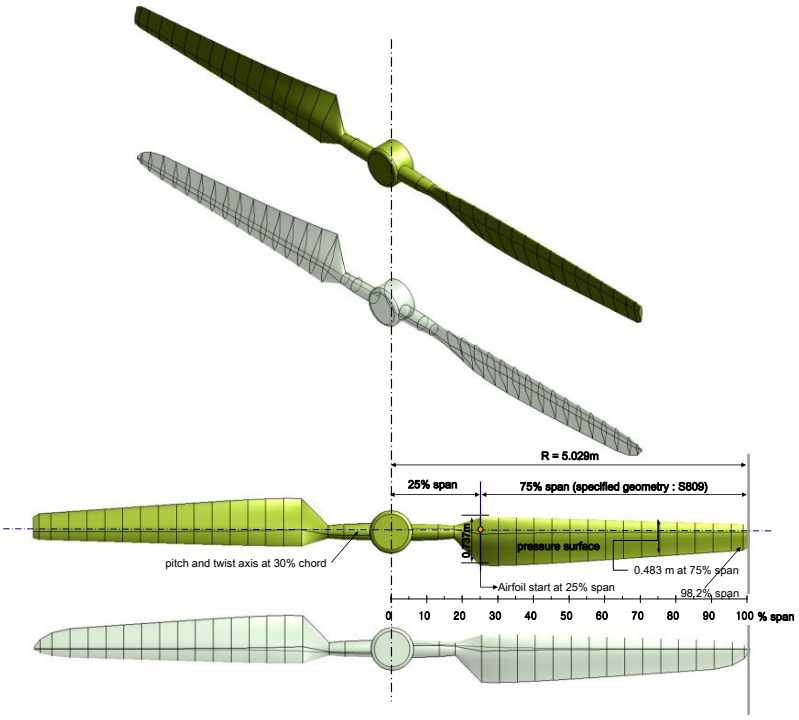

(**a**)

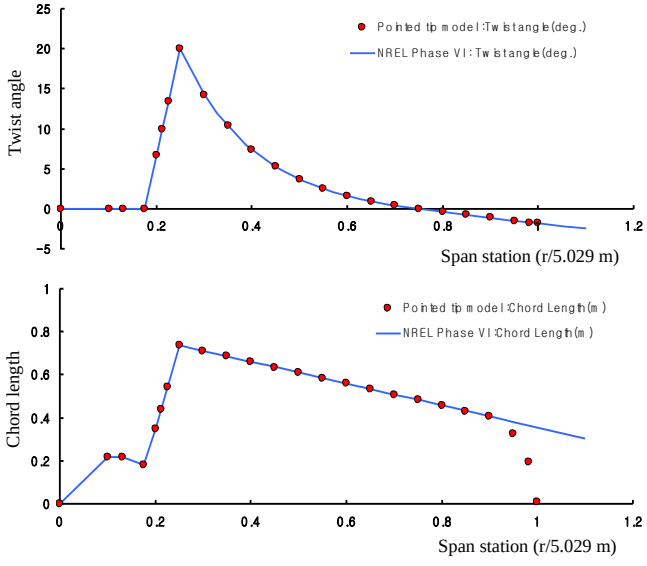

(**b**)

Figure 3. *Cont.*

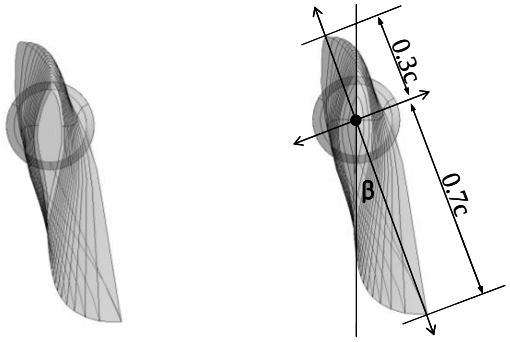

(**c**)

Figure 3. Geometry of NREL Phase-VI pointed tip blade: 3D pointed tip blade, twist, taper and side views. (**a**) NREL original Phase-VI blade and modified pointed tip blade; (**b**) twist angle and taper distribution along the blade span; and (**c**) side view of original and pointed tip NREL Phase VI blade.

A rectangular computational domain was generated for the CFD simulation, to determine the flow behavior around the blade. To find the optimum domain size, several domains with varying sizes were generated. The domain used in this work was considered optimum through comparative studies. A cylindrical domain was also generated around the blade within the rectangular domain as shown in Figure 4.

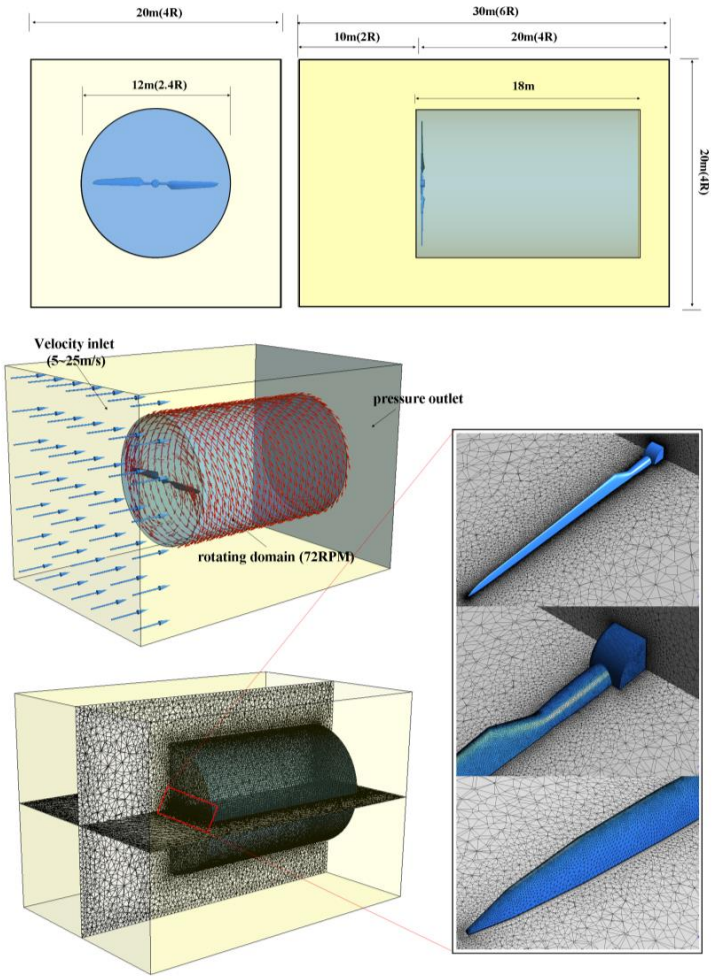

Figure 4. Computational fluid domain definitions with its full dimension.

This cylindrical domain is a rotating one which elucidates the blade-rotation phenomena. The rest of the rectangular domain remained fixed to represent the fixed-airflow condition. An interface connected the rotating and the fixed domain. The angular rotational speed of 72 rpm is used for the circular domain. The commercial software ANSYS was used for the blade design, simulation, and generation of results. The blade was modeled using a geometry modeler and divided into 16 sections.

An unstructured grid was generated along the domain for the CFD calculations. The accuracy of the calculation greatly depends on the quality of the grid. Approximately six million nodes were generated in near-wall mesh to keep the grid size sufficiently small which gives proper Y+ value of less than one. This fine mesh is important to get proper boundary wall condition. Y+ values more than 30 and 150 were also tested which failed to predict the near wall flow conditions accurately.

To define the boundary conditions, the rectangular front side was defined as the inlet, and the opposite end was defined as the outlet. All other surfaces of the rectangular domain were considered symmetric. The boundary condition of the blade was defined as wall. For the interface between the circular and the rotating domain, a mixing frame was considered.

The ANSYS CFX solver was used for the numerical calculations. CFX employs the Reynolds Average Navier–Stokes equation to solve fluid flow problems. To obtain a high accuracy, high-resolution solver control criteria were selected. The simulations were performed using the SST Gamma-Theta turbulent model, which predicts the transition, separation, and stall effect. To perform the calculation for several velocities, the inlet wind speed was varied. The results were collected from a post-processor.

3. Turbulent-Transition Model

The fundamental basis of CFD is the Navier–Stokes equation. Various turbulence equations are incorporated using this equation to solve engineering problems in several fields. In this current work SST Gamma-Theta turbulence model is used to predict near wall separation and transition effects on the boundary wall.

The SST turbulence model was formulated to predict the separation effect more accurately. This model combines the k-ε and k-ω models via the blending function. First, k-ω turbulence model equations were developed to improve the near-wall formulation of k-ε, which can predict either the near-wall effect or the turbulent-length scale in an adverse pressure gradient [19]. However, they exhibit a high sensitivity to the solution in the free-stream region outside of the boundary layer. A variation to these model equations that combines both equations was proposed as the SST turbulent model by Menter [19]. Although this model predicts both near-wall and larger-scale boundary effects, it is inaccurate for the viscous-sub-layer formulation and transitional flow and it sometimes bypasses the transitional effect. To overcome this, a new correlation-based model called the SST Gamma-Theta turbulent model [20,21] was introduced. This model was employed in this work owing to its better prediction capability of the stall, separation, and transition during boundary and turbulence effects compared to other available models [20,21].

The goal of developing the Gamma-Theta transition model was to develop a transition model based on local variables that could be easily implemented using modern CFD code with unstructured grids and massive parallel execution. The Gamma-Theta transition model has two equations also combined with the two ω-based equation turbulence models (SST, Baseline (BSL)). Transitional onset Reynolds number is one of the key formulas. The blending function used in this equation, which is zero in the free stream and one in the boundary layer is to take into account the diffusion from free stream. To trigger the boundary layer transition, the correlation based intermittency is done on transition onset.

In the SST Gamma-Theta turbulence model, the coupling of transition to turbulence model has been incorporated. This increases the robustness of the model by predicting the separated flow transition and also the effects of high-free-stream turbulence levels on buffered laminar boundary layers, so the SST Gamma-Theta turbulence model can describe the free stream intermittency and also can describe the change of shear stress. It helps to understand the flow which changes from laminar to

turbulence by using blending function. This blending function of Gamma-Theta turbulence model makes better understanding of the transitional effect.

4. Results and Discussion

Results were generated for five span-wise sections under various wind speed conditions. They are: (i) the pressure coefficient (C_p) distribution in all five sections of the blade for different wind speeds; (ii) wind-speed contour of the entire blade (top and front views); (iii) normal and tangential forces along the span of the blade; (iv) integrated torque and thrust forces; and (v) streamline flow distribution on the suction and pressure sides of the blade surface. The Reynolds number is calculated based on chord length of 1 m. The wind speeds considered were 7, 10, 13, 15, 20 and 25 m/s. The rotational speed considered is 72 rpm (ω = 7.5 rad/s) which corresponds to tip speed ratio of 1.5–7.5. The design wind speed is 7.2 m/s and tip speed ratio is 5.2 based on wind blade radius of 5.029 m and rpm of 72. The results were compared with the CFD and experimental results for the original NREL blade.

4.1. Stall Definitions

Figure 5 shows the lift (C_l) and drag (C_d) coefficients as a function of the angle of attack (AOA for four different Reynolds numbers: Re = 1,500,000, 1,250,000, 1,000,000, and 750,000, corresponding to wind speeds of 25, 20, 15, and 10 m/s, respectively. These values are obtained from the NREL experimental results of S809 airfoil. C_l and C_d values are plotted with AOA, ranging from −20° to 40°. The figure shows that the value of C_L increases almost linearly from 0° to 7° AOA indicating a fully attached flow region, then flattens out and reaches a peak value at an AOA of about 15°. In this region the flow experiences onset of separation and transition. From AOA values of about 15°–20° the C_l decreases from a maximum to a minimum value. This region is called the dynamic stall region and is shown as a pink rectangular box. From 20° to 40° the flow is fully detached and is called the deep stall region.

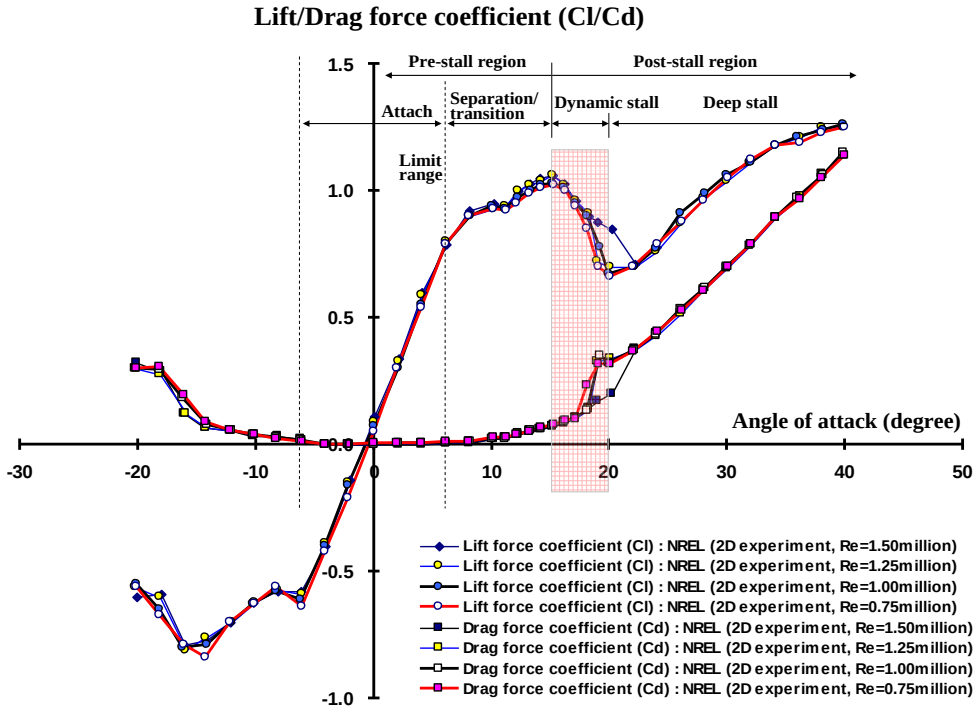

Figure 5. Lift and drag coefficient at different angle of attack for 2D S809 airfoil at various Reynolds number and the change of stall region with angle of attack.

Figure 6 shows the 3D span-wise AOA variation of the NREL blade with appropriate twist at varying wind speeds with constant RPM. At different wind speeds, the AOA changes along the span of the blade. At higher wind speeds near the hub region, the AOA is relatively high even with the high twist angle. The rectangular box in Figure 6 indicates the dynamic-stall region. At a wind speed of 5 m/s, the flow remains attached because the AOA along the entire span remains low. The blade span-wise AOA is slightly higher at a wind speed of 7 m/s, but is below the stall region; however, separation and transition may occur. At a wind speed of 10 m/s, the AOA increases above 20° in the hub region. The stall onset of full separation at 20° AOA occurs between the hub and the tip at near 46.7% span where the flow is fully separated from the leading edge to the trailing edge. The blade remains in the dynamic-stall condition up to 80% span. It also faces the stall onset of full separation at 20° AOA near the mid-span and near-tip regions at wind speeds of 13 and 15 m/s respectively. Thus, the 10 m/s wind speed can be defined as onset of the stall wind speed. The dynamic-stall region is defined by the wind-speed range of 10 to 15 m/s. At higher speeds of 20 and 25 m/s, flow on the whole blade span remains fully separated, indicating a very high AOA. This region is defined as deep-stall wind speed region.

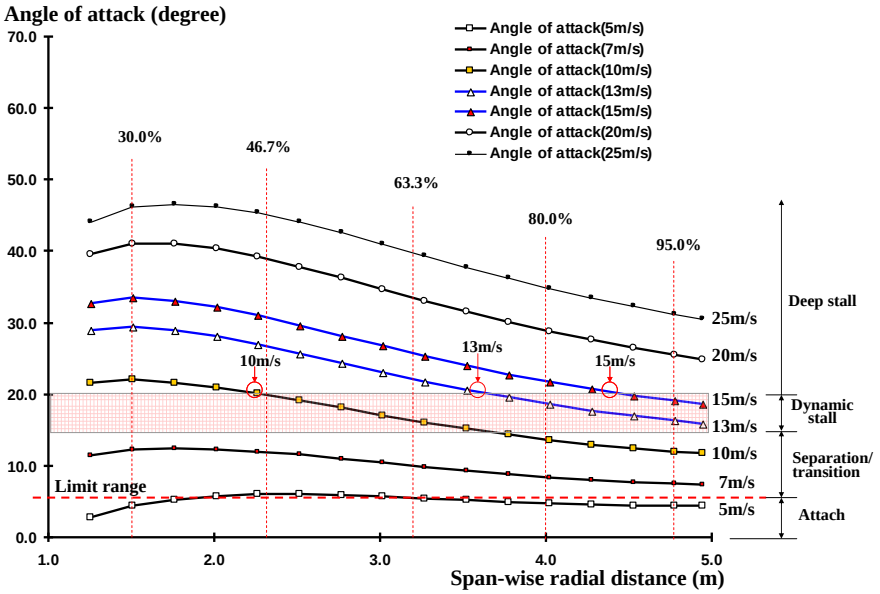

Figure 6. Span wise angle of attack distribution at various wind speeds, 20 degree stall onset for 3D blade and its relationship with 2D stall location.

4.2. Pressure Coefficient, Velocity and Pressure Contours

The pressure coefficient C_p is a non-dimensional pressure distribution along the chord of the airfoil. C_p is defined as the ratio of the difference in static and free stream pressures and the dynamic pressure. C_p is plotted upside-down with negative values (suction) on the top part of the plot. It starts from the stagnation point near the leading edge, changes suddenly on both upper and lower surfaces and finally recovers to a small positive value near the trailing edge.

Figure 7 represents the distributions of the pressure forces on five different sections of the blade at several wind speeds. Five m/s and 7 m/s are the low wind speed range. At this wind speed blade span AOA remains in the pre stall region. Blade span AOA is mainly in attached flow region at 5 m/s wind speed where the flow remains attached along the entire span. This result is similar for pointed tip blade and original NREL blade. The same phenomenon happens at a wind speed of 7 m/s. At high wind speeds of 20 and 25 m/s the flow is completely separated. As a result very little variation was observed between these two speeds. Therefore the results for low wind speed cases (5 and 7 m/s) and one of the high wind speed cases, 25 m/s, are not included in the discussion.

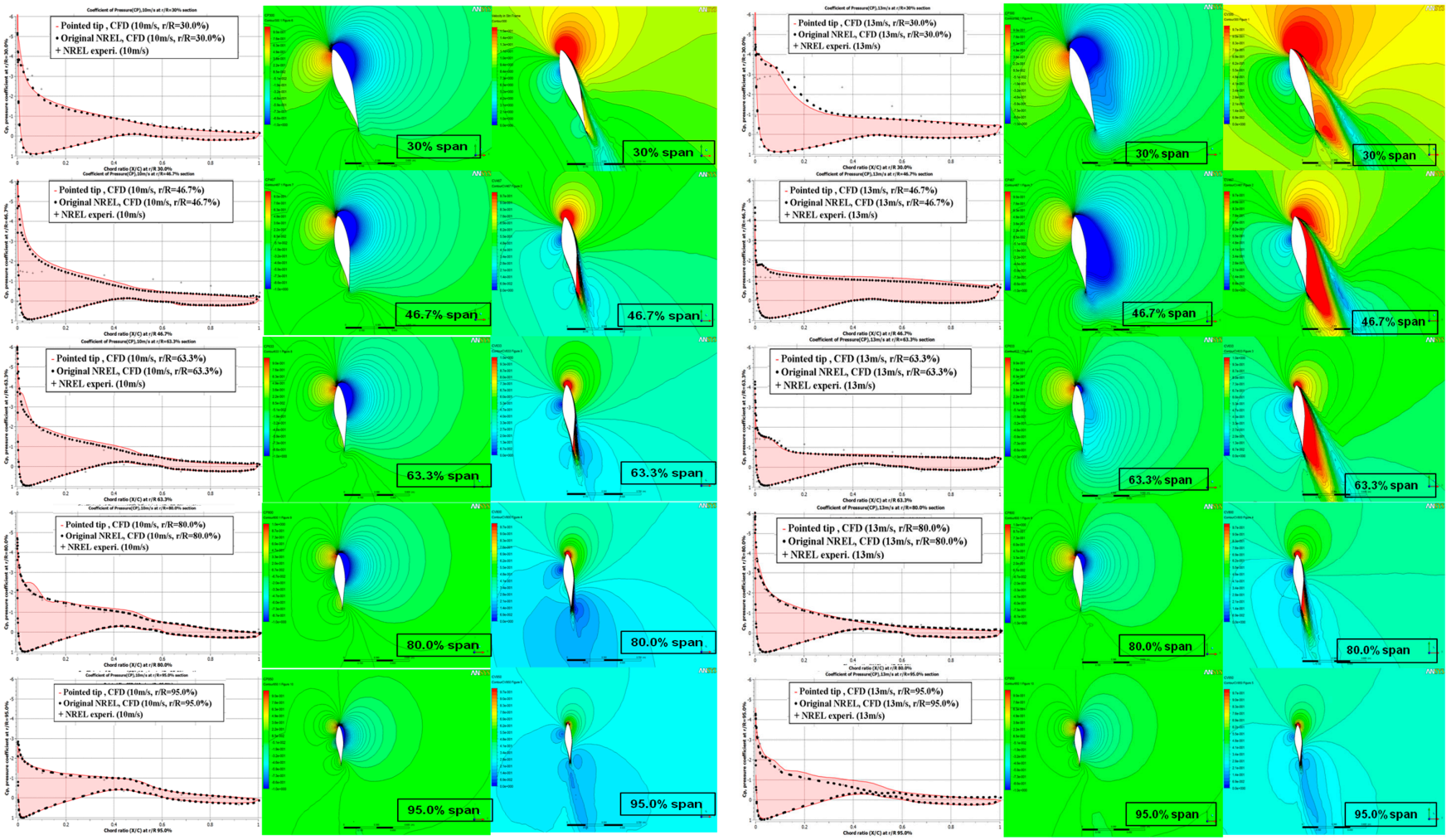

<C_p curve> <pressure contour> <velocity contour>

(**a**)

<C_p curve> <pressure contour> <velocity contour>

(**b**)

Figure 7. *Cont.*

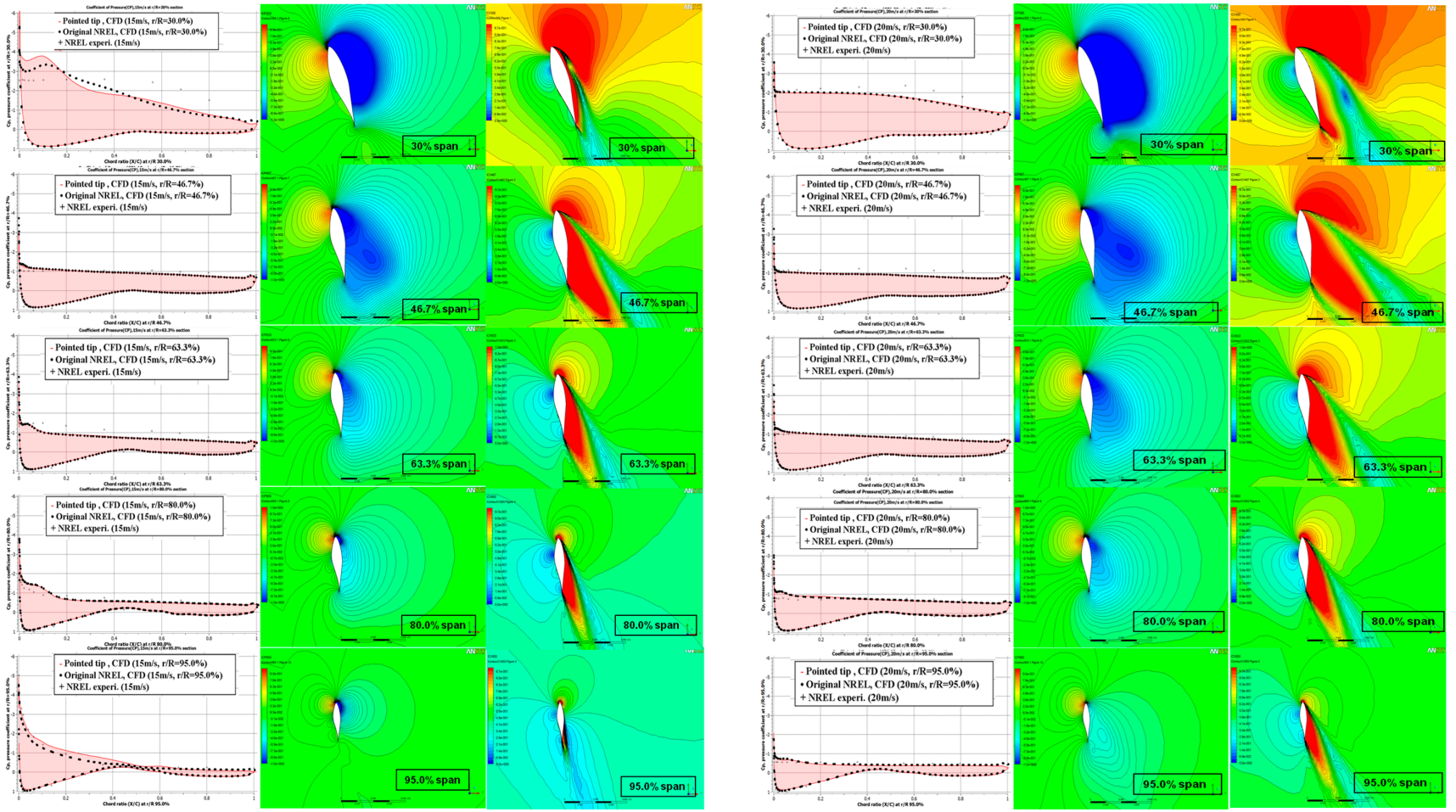

<C_p curve> <pressure contour> <velocity contour>

(**c**)

<C_p curve> <pressure contour> <velocity contour>

(**d**)

Figure 7. Sectional Pressure coefficient (C_p), pressure and velocity contour distribution at different wind speeds for pointed tip blade. (**a**) 10 m/s (**b**) 13 m/s; (**c**) 15 m/s; and (**d**) 20 m/s wind speed.

Wind speed-10 m/s: The span-wise AOA starts to increase to dynamic stall and deep stall regions at 10 m/s wind speed. Between 46.7% to near 80% span location the blade remains in the dynamic stall region. At 46.7% span the blade faces the onset of full separation of 20° AOA. At the leading edge, 30%–63.3% of blade span, the C_p curve of the pointed-tip blade is found to be higher than that of the NREL blade. This is because of the effect of the onset of stall and dynamic stall. After this span, the rest of the blade up to hub remains in deep stall region. Due to the stall effect flow starts to separate from the blade surface at around 63.3% span location. At this wind speed, the C_p distribution of pointed-tip blade starts to deviate from that of the original NREL blade because of the pointed tip shape effect as shown in Figure 7a. The pointed tip shape reduces the turbulent flow near the tip and affects the separated flow on the whole blade span.

Wind speed-13 m/s: At a wind speed of 13 m/s (Figure 7b), flow separation on the blade starts at 80% span, i.e., the separation point moves towards the tip. The 20° AOA, which is the onset of fully separated flow, occurs on the mid span. The rest of the blade up to the hub is in the deep-stall region where flow is fully separated. Thus, the variation in the C_p distribution of the pointed-tip blade with respect to experimental and CFD results for the original NREL blade shape starts in the same region. The C_p at 30% span of the blade show large discrepancies compared with the C_p of the experimental results. Near the tip at 95% span there is some discrepancy between pointed tip and original NREL blade C_p distributions which is due to pointed tip shape effect on the flow separation.

Wind speed-15 m/s: At 15 m/s wind speed the blade span AOA near the hub become high enough to be in deep stall region (Figure 6), so flow gets fully separated from the hub to 80% span location as shown in Figure 7c. It also faces the onset of full separation of 20° AOA at 90% span location. Flow has some transitional effect at 95% span location of the blade due to dynamic stall effect. As a result near the tip region C_p distribution deviates from the original NREL blade result due to its pointed tip effect on the transitional flow condition.

Wind speed-20 m/s: 20 m/s is high wind speed at which blade span AOA become high enough to be in deep stall region along the entire span Figure 7d. In this deep stall region flow gets totally separated from the leading edge towards the trailing edge of the blade surface. In every section of the blade the flow gets fully separated. Therefore the variation of the aerodynamic force between the original blade and pointed tip blade is negligible.

4.3. Sectional Flow Contour Around the Blade

Front and top views of the velocity contours of both the NREL and the pointed-tip blade are shown in Figure 8 for comparison for the five different wind speed cases. At the wind speed of 7 m/s, the flow was similar for both cases. Flow separation mainly starts at 10 m/s wind speed near 46.7% span location. The effect of onset of stall at this wind speed is responsible for this change. From the top view it is found that at low wind speeds such as 7 m/s, the flow pattern remains uniform after it passes over the blade. When the wind speed increases to 10 m/s, a wake starts to form while the flow passes the blade. Therefore it is expected that changes of aerodynamic force between the original blade shape and pointed tip blade at 7 m/s wind speed will be negligible. The variation starts to show at 10 m/s and higher.

At the wind speed of 13 m/s, the flow turbulence is higher than the previous wind speeds. A change in the flow pattern is observed near the hub and tip at the trailing edge which is the effect of stall onset of full separation of 20° AOA. Flow separation spreads from hub towards the tip at 15 m/s wind speed. As the wind speed increases, the 20° AOA shifts to near the tip. This results in full separation of the flow on the blade surface. The flow remains attached only near the tip region. There is negligible change near the tip for both blade shapes. The wind speeds of 13 and 15 m/s yield a high wake, as well as the separation of the flow from the blade surface, so the aerodynamic forces at this region for the pointed-tip blade are expected to be similar to those of the NREL blade. At the higher wind-speed of 25 m/s, the flow fully separates from the blade surface, and the whole blade

span remains in the deep-stall region. From a top view, the flow is found to be totally scattered, and the separation rate is high. Little variation in the flow condition for all wind speed cases was observed between the pointed-tip blade and the CFD results for the original NREL blade.

In CFD simulations, the Y+ effect is an important phenomenon for obtaining good predictions and results. Y+ is kept less than one for all the calculations at different wind-speed conditions. This value of less than one allows us to accurately predict the near-wall flow effects of the separation and transition. The Y+ values are kept less than one for both the original NREL blade and the pointed-tip blade.

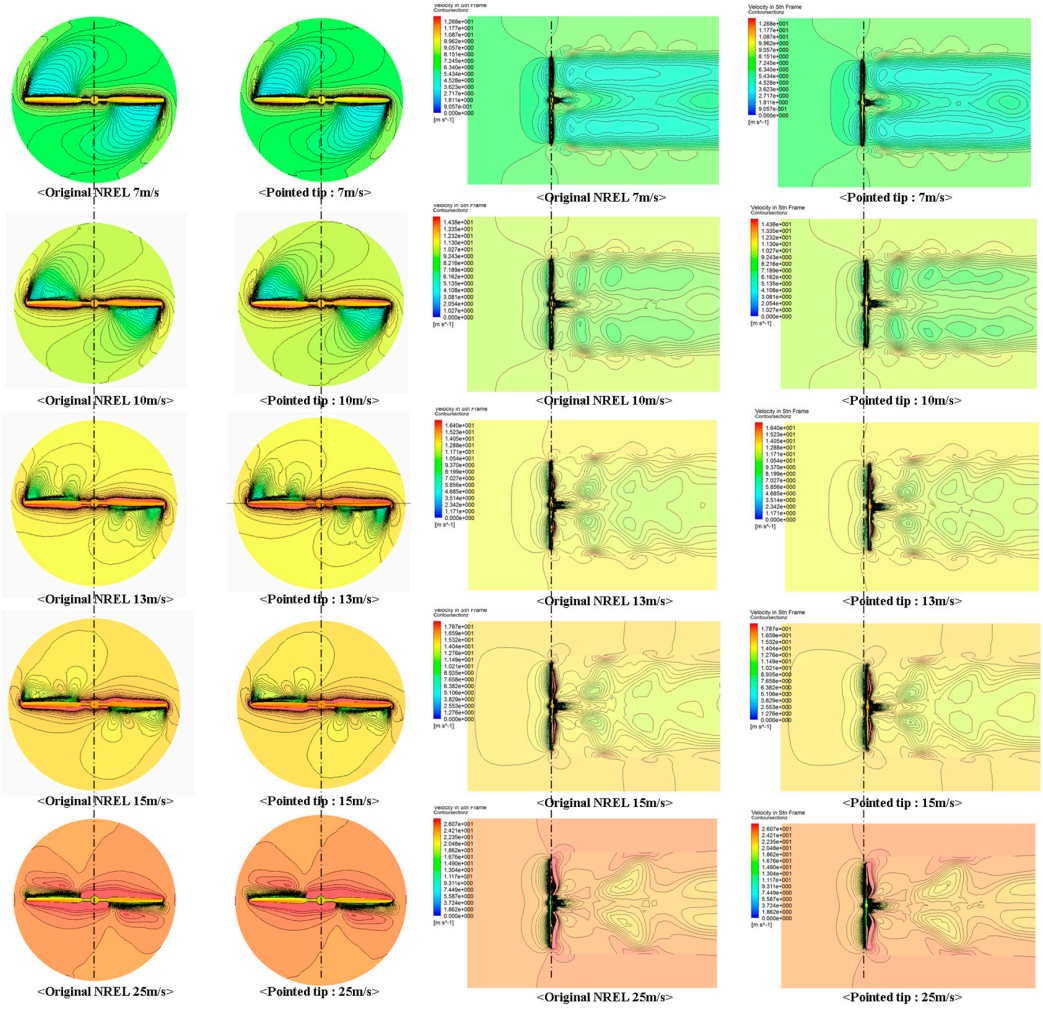

Figure 8. Sectional front and top flow contours around the blade at different wind speeds. (**a**) Front view; and (**b**) top view.

4.4. Aerodynamic-Force Coefficient

At the wind speed of 5 m/s, the tangential-force coefficient of the pointed-tip blade exhibits very little discrepancy with the experimental and CFD results for the original NREL blade as shown in Figure 9a. It has a smooth, slightly concave curve. The flow is perfectly attached to the blade because the whole blade span AOAs are low at this wind speed. As a result the difference in aerodynamic force between two blade shapes is negligible. There is slight decrease in normal force near the tip compared to original NREL blade as shown in Figure 9a. This is expected because of the decreased area of the shape near the tip.

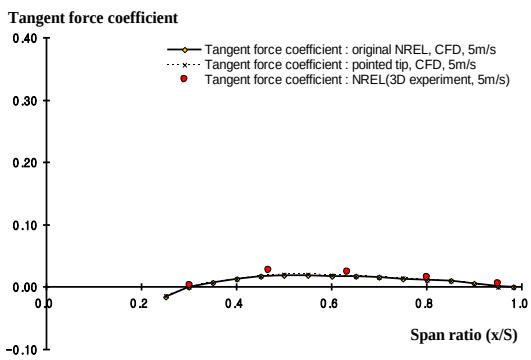

<Tangential force coefficient along the span>

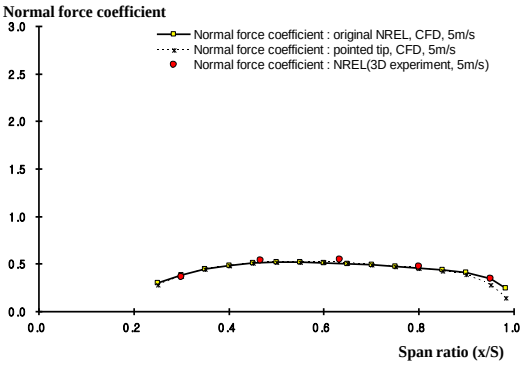

<Normal force coefficient along the span>

(**a**)

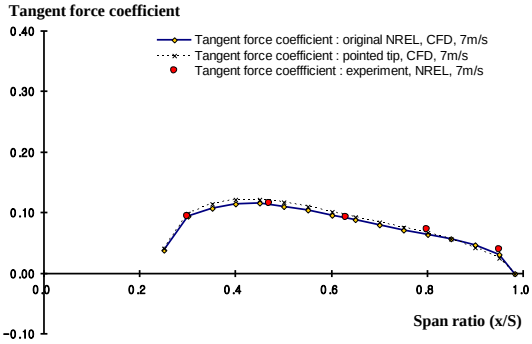

<Tangential force coefficient along the span>

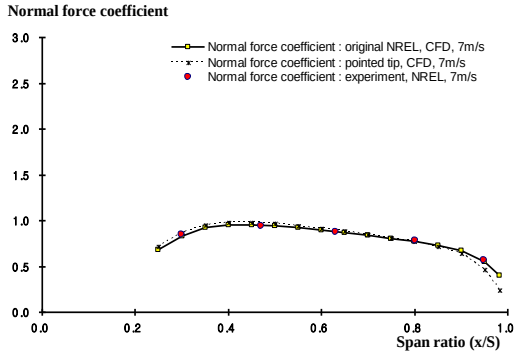

<Normal force coefficient along the span>

(**b**)

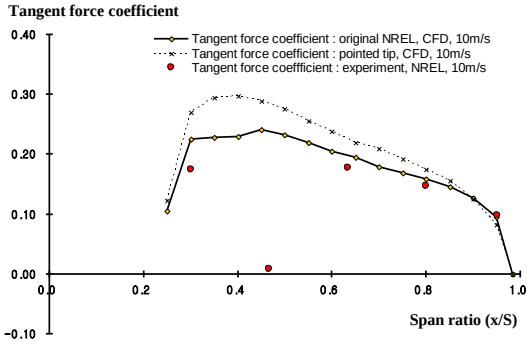

<Tangential force coefficient along the span>

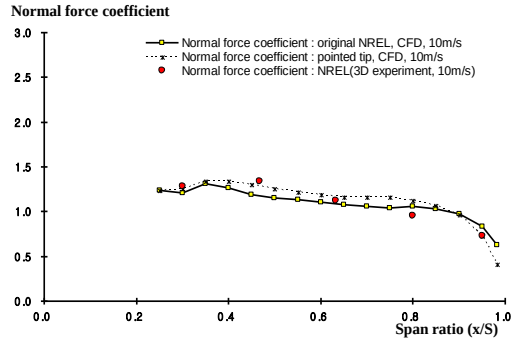

<Normal force coefficient along the span>

(**c**)

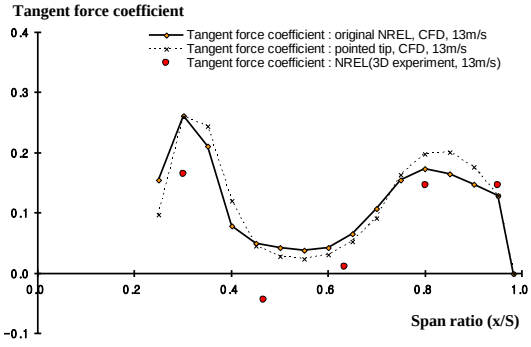

<Tangential force coefficient along the span>

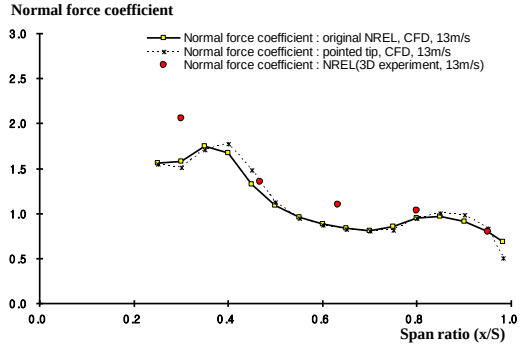

<Normal force coefficient along the span>

(**d**)

Figure 9. *Cont.*

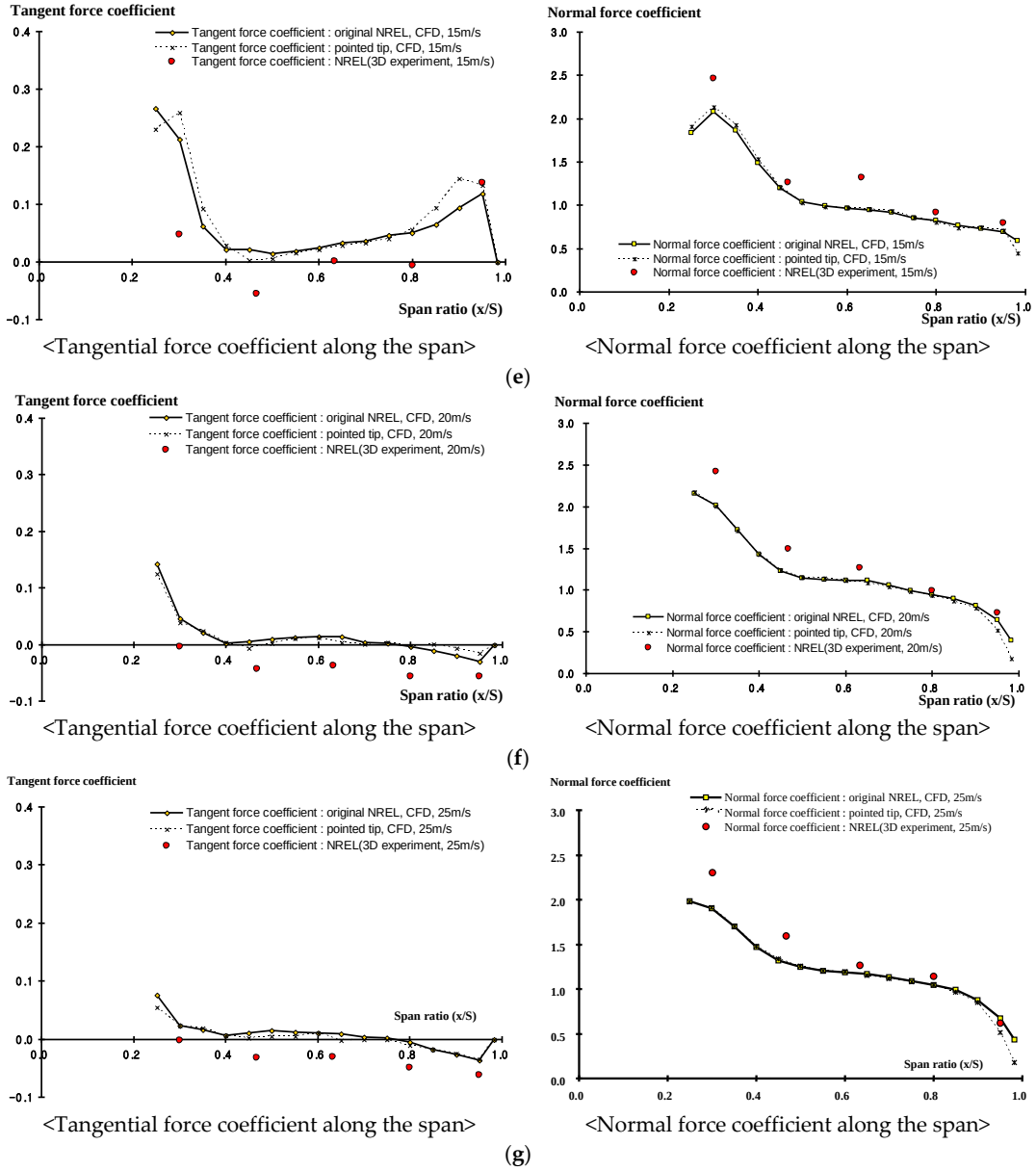

Figure 9. Sectional tangential and normal force coefficient at different wind speed for both the pointed tip and NREL Phase VI blades. (**a**) 5 m/s; (**b**) 7 m/s; (**c**) 10 m/s; (**d**) 13 m/s; (**e**) 15 m/s; (**f**) 20 m/s; and (**g**) 25 m/s wind speed.

At 7 m/s, as previously discussed, the blade-span AOAs are slightly higher than the 5 m/s but still the entire blade remains in the pre-stall region—inducing only a transitional effect on the blade. The major flow remains attached. Thus, the tangential force coefficient is slightly higher than 5 m/s wind speed as shown in Figure 9b. The results show small variation between the two blades. The tangential force of the pointed tip blade is slightly over predicted, at around 46.7% section, compared to the NREL blade because of the higher C_p near the leading edge. There is negligible deviation in the normal force coefficient between the pointed-tip blade and original NREL blade because this coefficient has a smaller dependency on the near wall flow behaviors. The irregular flow separation on the suction side greatly affects the tangential force coefficient but not the normal force coefficient.

Tangential force coefficients are significantly overpredicted by the CFD simulations both for pointed-tip blade and original NREL blade shape at a wind speed of 10 m/s compared to the NREL

experimental data as shown in Figure 9c. In experimental results the NREL blade tangential force drops due to the stall effect but this cannot be predicted in CFD simulations due to stall delay. The C_p distribution at this wind speed for the pointed tip blade is higher than in the NREL blade results at 46.7% span of the blade which is the onset of full separation of 20° AOA (Figure 6). The blade also faces a dynamic stall effect due to which the tangential force coefficient for the pointed tip blade is found to be higher than for the NREL blade. This higher tangential force coefficient value does have a beneficial effect on the torque. The change in the normal force coefficient, as shown in Figure 9c, is not significant at 10 m/s wind speed. The only deviations are observed as expected at the tip. This lower value at the tip has an effect on deflection of the blade. In the mid span, force is higher than the NREL blade which may not influence the total value of normal force coefficient.

The tangential force coefficient along the span suddenly decreases at 13 m/s wind speed as shown in Figure 9d. This is because the C_p value also decreases at 46.7% span. As described in Figure 6, at this wind speed the blade span AOA near hub remains in the deep-stall region which causes a high separation of flow along the span. The tangential force coefficient again increases at 80% span, where the sectional AOA is in the dynamic-stall region. This is where the separation and transitional flow occur. Near the tip, due to the critical stall onset of the full separation effect of 20° AOA, the value of the tangential force becomes higher than for the NREL blade, which is beneficial for torque force. This stall effect also has an influence on normal force coefficient of the pointed tip blade near the tip, where the values become lower than for the NREL blade.

As the wind speed increases to 15 m/s, the effect of stall becomes more prominent, which makes the decrease in the value of tangential force coefficient earlier than previous wind speed cases as shown in Figure 9e. Compared to NREL blade, the pointed tip blade has a higher tangential force coefficient value only near the tip (around 85% span) where the onset of full separation has taken place as indicated in Figure 9e. In the case of the normal force coefficient, there is only a small variation in the values between the two blade shapes.

The aerodynamic force coefficient characteristics for high wind speeds of 20 and 25 m/s are similar. At this wind speed the blade sectional AOAs are all in the deep-stall region where flow gets fully separated from the blade surface. Thus, the tangential force coefficients, as shown in Figure 9f,g, decrease to negative values from 80% span up to the tip for both blades. The C_p graph shows that the pressure variation is very small at every section. The tangential force coefficient distribution for the pointed tip blade agrees very well with the results of the original NREL blade because at high speed the flow is fully separated and thus the effect of blade shape is negligible. For the normal force coefficient, the effect of the reduced area of the pointed tip blade makes the value lower than for the NREL blade. This lower value will help in the stability of the blade.

4.5. Streamline Flow on the Blade Surface

The streamline flow distribution on blade surface helps predict the 3D flow behavior on the blade surface. Figure 10a,b present the suction side flow distribution on NREL and pointed tip blade, respectively. The well-organized vertical and sloping radial streamlines shown in the figures indicate the attachment and flow separation on the blade surfaces for all wind speeds, respectively. The color contour shows the wall shear stress.

At a wind speed of 5 m/s, flow is attached to the entire blade surface on the suction side as shown in Figure 10a,b. This phenomenon is similar for both blade shapes. Therefore the change of aerodynamic forces between the two blades at this wind speed is negligible as found earlier.

At a wind speed of 7 m/s, the blade-span AOA is higher than that in previous wind-speed cases, therefore separation and transition start to occur near the hub region on the suction side of both blades as shown in Figure 10. On the rest of the blade on the suction side, flow still remains attached. For the pointed-tip blade, the streamline flow is found to be more attached compared with those of the original blade as indicated in Figure 10a. This yields a slightly higher aerodynamic force at the 7 m/s wind speed.

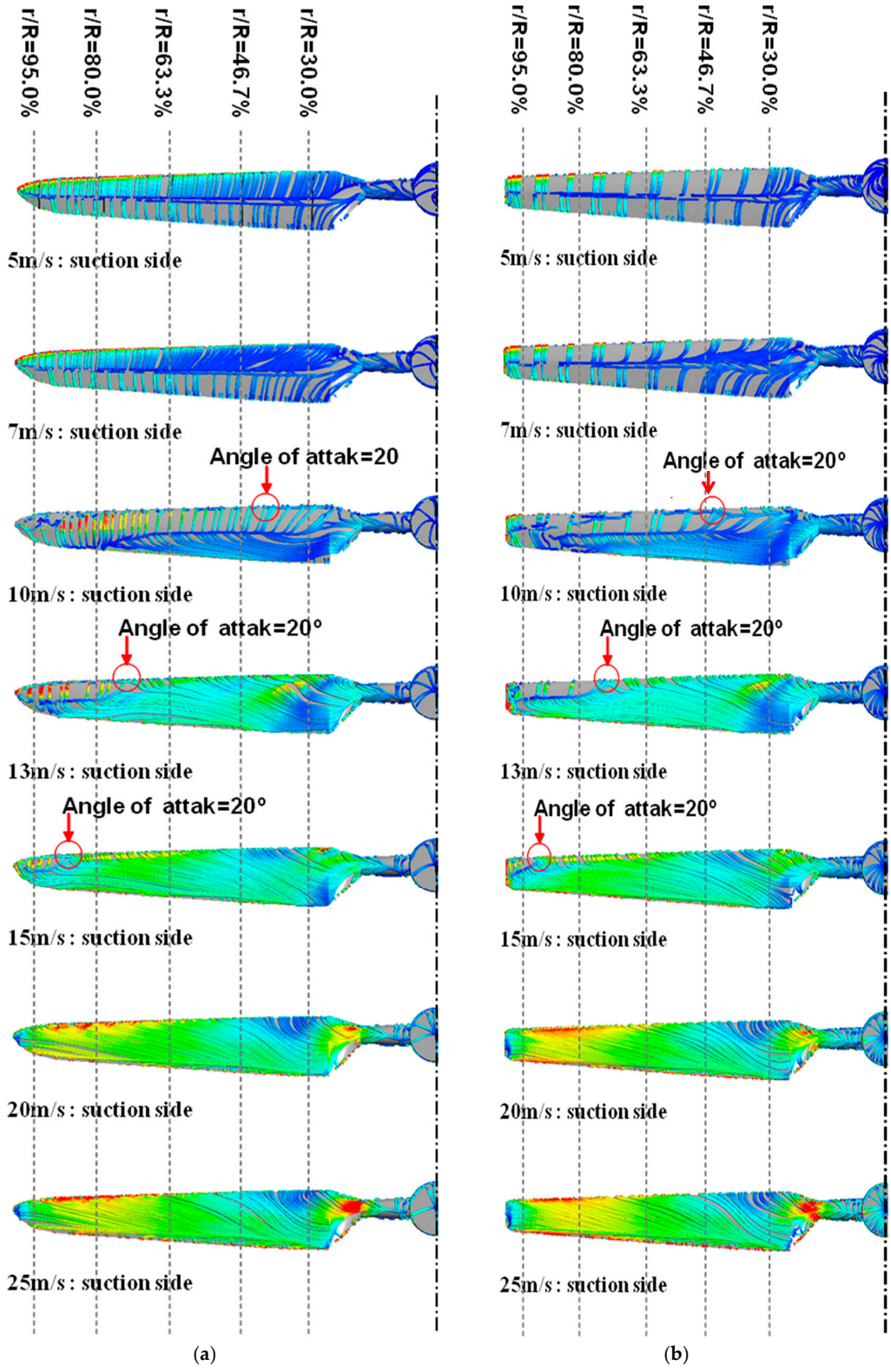

Figure 10. Change of streamline flow along the blade span of (**a**) pointed tip blade in various wind speed (suction side); and (**b**) NREL Phase-VI blade in various wind speed (suction side).

At a wind speed of 10 m/s, the blade span faces a higher AOA of the deep stall region near the hub. The flow mainly remains attached from the mid chord to the leading edge on the suction side of the blade, except near the hub and tip (Figure 10a). This is because at this wind speed 46.7%–80% span

of the blade is in dynamic stall region where flow transition occurs. The stall onset of full separation of 20 degree AOA is on the 46.7% span of the blade. Flow remains attached from 80% span up to the tip region. This attached flow is found to be more prominent on the pointed tip blade. This high attached flow characteristics on the tip and stall onset region are reflected in the values of aerodynamic force coefficient and hence the power curve. At a wind speed of 13 m/s, the flow-separation region on the suction side increases. This is influenced by the high AOA along the blade span. The regions from the hub to almost 63.3% span exhibit flow separation on blade suction side as shown in Figure 10a. Even the flow is separated on the trailing edge after 63.3%–95% span of the blade. Only a small streamline flow in the region near the tip remains attached. On 80% span of the blades where AOA is 20°, the trailing edge flow for the pointed tip blade is found to be more attached than in the NREL blade as shown in Figure 10a,b. This attached flow leads to a higher tangential force coefficient for the pointed tip blade.

At a wind speed of 15 m/s, the flow is almost fully separated throughout the blade except near the tip on the suction side. Due to deep stall effect the flow separation is high at this wind speed. Near the tip due to the shape effect flow attachment is less prominent for the NREL blade than for the pointed tip blade. Stall onset of full separation is near 90% span of the blade where flow attachment is high for the pointed tip blade. This higher attached flow also affects the aerodynamic forces which results in a higher tangential force coefficient of the pointed tip blade. In addition, the value of the normal force coefficient near the tip region of the pointed tip blade gives lower result than the other shape. This is better for stability of the blade.

When the wind speed increases to 20 m/s, the flow completely separates on the suction side. At this wind speed, the entire blade is in the deep-stall region, and there is fully separated flow on suction side because of the higher AOA. This is true at wind speeds of 20 m/s or higher for the pointed-tip blade and the original NREL blade. There is slight transitional effect on the pressure side at 80%–90% span. Flow is mainly attached at this side of the blade. In this case flow separation is high at suction side, which leads to reduced effect of the tip shape on aerodynamic forces. A similar streamline flow separation like 20 m/s wind speed is also observed at 25 m/s.

In the deep stall region of 20 and 25 m/s wind speeds flow is fully separated from the blade surface. This leads to a negligible effect of the pointed tip shape on the aerodynamic force coefficient. In low wind speed cases the change of aerodynamic force is also negligible. Only in the 10–15 m/s wind speed region where flow transitions occurs on the blade surface, the shape of the tip affects the aerodynamic forces. 10 m/s wind speed is considered as the stall wind speed due to blade span facing all the stall effects.

4.6. Torque and Thrust

The results for torque and thrust are presented in Figures 11 and 12 and compared with previously reported results for different wind speeds. The graphs of Figure 12 compare the simulated results for the pointed-tip geometry and the original NREL blade with SST Gamma-Theta turbulence models. They also show data from NREL experiments, BEM, vortex-method and several CFD simulations performed by other researchers.

The simulation shows excellent agreement at high wind speeds (20–25 m/s) and low wind speeds (5–7 m/s) but overpredicts in the medium speed range of 10 to 15 m/s, where the blade span faces the stall effect of transition of 20° AOA and dynamic stall effects.

At low wind speeds, the torque is similar for pointed-tip blade and the original NREL blade (Figure 11). This is because the blade overall span AOA is low and remains in the pre-stall region. Thus, there is no separation on the blade surface, and consequently, the tangential force is similar between the pointed-tip blade and the original NREL blade. Owing to the strong attachment of the flow at a wind speed of 7 m/s, the tangential-force coefficient is slightly higher for the pointed-tip blade compared with the original NREL blade, which helps to increase the torque.

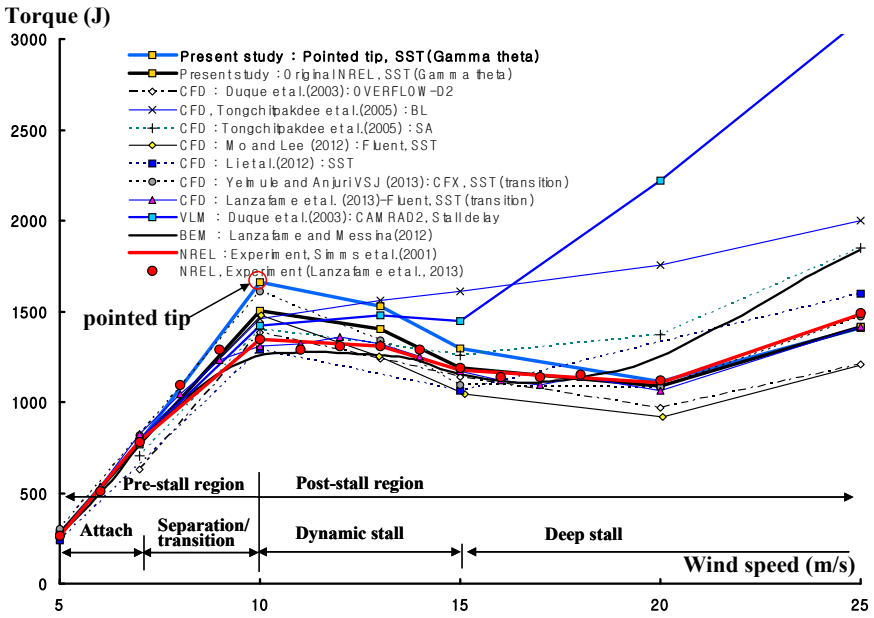

Figure 11. Comparison of torque from various research on NREL Phase-VI blade and pointed tip blade at different wind speed conditions and their relation with stall effect [5,11–13].

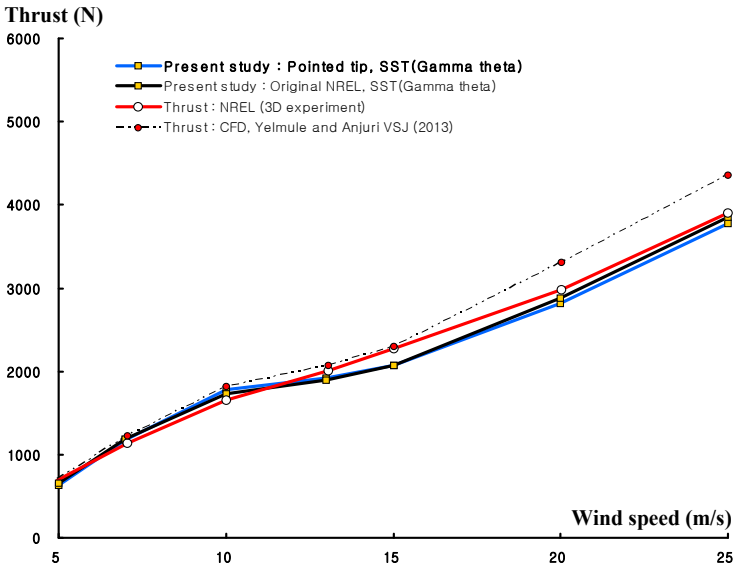

Figure 12. Comparison of thrust on NREL Phase VI blade and pointed tip blade with different wind speed conditions.

At a wind speed of 10 m/s, the blade faces the stall onset of 20° AOA at 46.7% of the span, where flow changes occur, which increases the tangential force. The tangential force is higher for the pointed-tip blade in this region because flow remains more attached for the pointed-tip blade than the original NREL blade. This yields around 8% higher torque for the pointed-tip blade compared with the original NREL blade at the 10 m/s wind speed. Thus, the power will also be high for the pointed-tip blade at this wind speed. At wind speeds of 13 and 15 m/s, the blade remains in the dynamic stall region. The stall-onset effect was observed in the region near the tip. For the pointed-tip blade, the flow is more strongly attached in the dynamic stall region compared with the original NREL blade which gives a higher tangential-force coefficient. Therefore, the torque of the pointed tip blade is higher than for the original NREL blade. Although the torque of the pointed tip is highest at a wind speed

of 10 m/s, it decreases at 15 m/s wind speed due to the stall-regulated nature of the NREL Phase VI wind turbine blade, but still remains higher than in the original blade. Because of the higher torque the pointed-tip blade exhibits better predictability and yields higher blade effectiveness than the original NREL blade. At a 20 m/s wind speed, the results between the two blades are similar. At 25 m/s, the torque for the pointed-tip blade matches the CFD results of the NREL blade. The variation of the results is negligible because at separation the effect of the tip is less. The thrust values with different wind speeds are presented in Figure 12. Our simulations for both the pointed-tip and original NREL blades are compared with the NREL experimental data and results from another simulation [18]. As expected, the simulations exhibit good agreement but underpredict the experimental data in the post stall region of 10–25 m/s wind-speed cases. At 13 and 15 m/s wind speeds, the CFD thrust forces for both pointed-tip and NREL blades are lower than the experimental results. At 20 m/s, this variation decreases. It is found that the pointed-tip blade yields a lower value of the thrust than the original NREL blade. This lower value of thrust force at high wind speeds is expected to be beneficial for the blade stability.

5. Conclusions

The aerodynamic forces on the pointed-tip blade were compared with the forces on the original NREL blade. It was found that pointed-tip blade yields better aerodynamic forces which would result in higher power than NREL blade. The SST Gamma-Theta turbulent model was selected as solver equation because it can successfully incorporate near-wall transitional-to-turbulent effects in the high-separation region with high-resolution of grid.

At low wind speeds (5–7 m/s cases), changes of aerodynamic forces between the pointed tip and NREL blade were found to be negligible. When the wind speed becomes 10 m/s, the blade faces the onset of full separation as well as the effect of dynamic stall. This is the region where flow transitions occur and the effect of the tip shape becomes prominent. As a result, the tangential force coefficient and hence the torque becomes about 10% higher compared to the NREL blade. The blade also faces similar effects at 13 and 15 m/s wind speed, which results in 8%–10% higher torque. At higher wind speeds of 20 and 25 m/s, flow gets totally separated due to the deep stall effect. Therefore, there is negligible change in aerodynamic force characteristics on both the blade shapes.

It is clear that in the dynamic stall region (10–15 m/s wind speed) where the separation induced transitional flow occurs, the pointed tip blade exhibits better aerodynamic force characteristic than the NREL blade. The torque value of the pointed tip blade becomes around 8%–10% higher than that of the NREL blade. In addition, the thrust force is reduced a little for the pointed tip blade, which results in higher power and better stability of the pointed tip blade compared to the NREL blade. The lower thrust force value at higher wind speed also gives the possibility of lower deformation of the tip. Therefore, it can be concluded that pointed tip blade has more advantages from the point of view of power production and also has the possibility of lower deflection than the NREL blade shape. In addition, the reduction of the shape may also help in structural stability which he hope to prove by structural analysis in future work.

Acknowledgments: This research was supported by the National Science Foundation (NSF) through the Center for Energy and Environmental Sustainability (CEES), a CREST Center (Award No. 1036593).

Author Contributions: Kyoungsoo Lee and Ziaul Huque conceived and designed the experiments; Kyoungsoo Lee and Shrabanti Roy performed the experiments; Kyoungsoo Lee, Ziaul Huque, Raghava Kommalapati and SangEul Han analyzed the data; Kyoungsoo Lee, Shrabanti Roy, Ziaul Huque and Raghava Kommalapati wrote the paper.

Conflicts of Interest: The authors declare no conflict of interest.

References

1. Sommers, D.M. *Design and Experimental Results for the S809 Airfoil*; Technical Report; National Renewable Energy Laboratory (NREL): Golden, CO, USA, 1997.

2. Ramsay, R.R.; Janiszewska, J.M.; Gregorek, G.M. *Wind Tunnel Testing of Three S809 Aileron Configurations for Use on Horizontal Axis Wind Turbines*; Technical Report; National Renewable Energy Laboratory (NREL): Golden, CO, USA, 1996.
3. Simms, D.; Schreck, S.; Hand, M.; Fingersch, L.J. *NREL Unsteady Aerodynamics Experiment in the NASA-Ames Wind Tunnel: A Comparison of Predictions to Measurements*; Technical Report; National Renewable Energy Laboratory (NREL): Golden, CO, USA, 2001.
4. Hand, M.; Simms, D.; Fingersch, L.J.; Jager, D.; Larwood, S.; Cotrell, J.; Schreck, S. *Unsteady Aerodynamics Experiment Phase VI: Wind Tunnel Test Configurations and Available Data Campaigns*; Technical Report; National Renewable Energy Laboratory (NREL): Golden, CO, USA, 2001.
5. Lanzafame, R.; Messina, M. BEM theory: How to take into account the radial flow inside of a 1-D numerical code. *Renew. Energy* **2012**, *39*, 440–446. [CrossRef]
6. Sharifi, A.; Nobari, M.R.H. Prediction of optimum section pitch angle distribution along wind turbine blades. *Energy Convers. Manag.* **2013**, *67*, 342–350. [CrossRef]
7. Tangler, J.L.; David Kocurek, J. *Wind Turbine Post-Stall Airfoil Performance Characteristic, Guidelines for Blade-Element Momentum Methods*; NREL/CP-500-369001; National Renewable Energy Laboratory (NREL): Golden, CO, USA, 2004.
8. Feszty, T.; Mc, D.S.; Nitzsche, F. *Aerodynamic Simulation of the NREL Phase VI Wind Turbine Using a Discrete Vortex Method Coupled with a Nonlinear Beam Model*; Department of Mechanical and Aerospace Engineering, Carleton University: Ottawa, ON, Canada, 2009.
9. Jonathon, S.; Sibuetrs, W.C.; Christian, M. CFD in wind energy: The virtual, multiscale wind tunnel. *Energies* **2010**, *3*, 989–1013.
10. Sezer-Uzol, N.; Long, L. 3-D time-accurate CFD simulations of wind turbine rotor flow fields. In Proceedings of the 44th AIAA Aerospace Sciences Meeting and Exhibit, Reno, NV, USA, 9–12 January 2006.
11. Duque, E.P.N.; Burklund, M.D.; Johnson, W. Navier-Stokes and comprehensive analysis performance predictions of the NREL phase VI experiment. *J. Sol. Energy Eng.* **2003**, *125*, 457–467. [CrossRef]
12. Tongchitpakdee, C.; Benjanirat, S.; Sankar, L.N. Numerical simulation of the aerodynamics of horizontal axis wind turbines under yawed flow conditions. *J. Sol. Energy Eng.* **2005**, *127*, 464–474. [CrossRef]
13. Yelmule, M.M.; Anjuri, E.V.S.J. CFD predictions of NREL Phase VI rotor experiments in NASA/AMES wind tunnel. *Int. J. Renew. Energy Res.* **2013**, *3*, 250–260.
14. Mohammad, M.; Song, Y.J.; Xie, Y.H. Effects of near-wall grid spacing on SST-K-ω model using NREL Phase VI horizontal axis wind turbine. *J. Wind Eng. Ind. Aerodyn.* **2012**, *107–108*, 94–105.
15. Ferrer, E.; Munduate, X. Wind turbine blade tip comparison using CFD. *J. Phys. Conf. Ser.* **2007**, *75*, 012005. [CrossRef]
16. Helge Aagaard, M.; Peter, F. *Numerical Simulation of Different Tip Shapes for Wind Turbine Blade*; Riso-R-891(EN); Risq National Laboratory: Roskilde, Denmark, 1996.
17. Jeppe, J.; Niels, S.N. *Numerical Investigation of Three Wind Turbine Blade Tips*; Risq-R-1543(EN); Risø National Laboratory: Roskilde, Denmark, 2002.
18. Jeppe, J.; Niels, N.S. *Aerodynamic Investigation of Winglets on Wind Turbine Blades Using CFD*; Risq-R-1543(EN); Risø National Laboratory: Roskilde, Denmark, 2006.
19. Menter, F.R. Two-equation eddy-viscosity turbulence models for engineering applications. *AIAA J.* **1994**, *32*, 1598–1605. [CrossRef]
20. Menter, F.R. Review of the shear-stress transport turbulence model experience from an industrial perspective. *Int. J. Comput. Fluid Dyn.* **2009**, *23*, 305–316. [CrossRef]
21. Menter, F.R.; Langtry, R.; Völker, S. Transition modelling for general purpose CFD codes. *Flow Turbul. Combust.* **2006**, *77*, 277–303. [CrossRef]
22. Giguere, P.; Selig, M.S. *Design of a Tapered and Twisted Blade for the NREL Combined Experiment Rotor*; NREL/SR-500-26173; National Renewable Energy Laboratory: Golden, CO, USA, 1999.